RESEARCH ARTICLE

Structural reliability assessment of offshore wind turbine support structures subjected to pitting corrosion-fatigue: A damage tolerance modelling approach

Abdulhakim Adeoye Shittu[1,2] ⓘ | **Ali Mehmanparast**[1] ⓘ | **Mahmood Shafiee**[3] ⓘ |
Athanasios Kolios[4] ⓘ | **Phil Hart**[1] | **Karl Pilario**[1,5] ⓘ

[1]Department of Energy and Power, Cranfield University, Cranfield, MK43 0AL, United Kingdom

[2]Department of Mathematics and Statistics, Federal University Wukari, Wukari, Taraba, Nigeria

[3]School of Engineering and Digital Arts, University of Kent, Canterbury, CT2 7NT, United Kingdom

[4]Department of Naval Architecture, Ocean and Marine Engineering, University of Strathclyde, Glasgow, G1 1XQ, United Kingdom

[5]Department of Chemical Engineering, University of the Philippines Diliman, Quezon City, Philippines

Correspondence
Ali Mehmanparast, Department of Energy and Power, Cranfield University, Cranfield, UK.
Email: a.mehmanparast@cranfield.ac.uk

Abstract

The structural integrity of offshore wind turbine (OWT) support structures is affected by one of the most severe damage mechanisms known as pitting corrosion-fatigue. In this study, the structural reliability of such structures subjected to pitting corrosion-fatigue is assessed using a damage tolerance modelling approach. A probabilistic model that ascertains the reliability of the structure is presented, incorporating the randomness in cyclic load and corrosive environment as well as uncertainties in shape factor, pit size and aspect ratio. A non-intrusive formulation is proposed consisting of a sequence of steps. First, a stochastic parametric Finite Element Analysis (FEA) is performed using SMART© crack growth and Design Xplorer© facilities within the software package ANSYS. Secondly, the results obtained from the FEA are processed using an Artificial Neural Network (ANN) response surface modelling technique. Finally, the First Order Reliability Method (FORM) is used to calculate the reliability indices of components. The results reveal that for the inherent stochastic conditions, the structure becomes unsafe after the 18th year, before the attainment of the design life of 20 years. The FEA results are in very good agreement with results obtained from analysis steps outlined in design standard BS 7910 and other references designated as 'theoretical analysis methods' in this study. The results predict, for the case study, that the pit growth life is approximately 56% of the total pitting corrosion fatigue life. Sensitivity analysis results show that the aspect ratio of pits at critical size plays a significant role on the reliability of the structure.

KEYWORDS

artificial neural network, non-intrusive formulations, offshore wind structures, pitting corrosion fatigue, reliability index, structural reliability analysis

1 | INTRODUCTION

Renewable energy technologies are now widely deployed in many parts of the world, including Europe, China, and United States.[1] Wind energy is a technically and economically feasible option to partially address the global issues related to the energy crisis and climate change. The majority of wind energy is harnessed by onshore wind farms,[2] despite regular local opposition due to visual and sound impacts. A solution is to deploy wind turbines at sea thus minimizing sound and visual impact, with additional capacity factor benefits obtained from the improved wind domain due to unobstructed fetch. This has led to the increasing development of offshore wind industry, especially in Europe where the offshore wind energy capacity is expected to reach 64.8 GW by 2030.[1,3–7]

Most of the existing offshore wind turbines (OWTs) use monopile foundations and are installed in water depths less than 50 m. However, for larger turbines in deeper waters, monopiles become very large and increasingly uneconomical due to the difficulty of fabricating and installing such systems, as well as the consideration of modal requirements. More information on monopile foundations can be found in Wang et al.[8,9] To address these issues, space frame structures such as jackets are used, which have lighter weight and are stiffer than monopiles. Space frames can be cheaper in deep-water circumstances, and hence, they can contribute to the offshore wind industry's goal on the reduction of levelized cost of energy (LCoE). However, designing these structures effectively is resource-intensive, especially when designing to withstand the wide set of dynamic loading mechanisms. Thus, research is still required to improve the design and analysis of jacket type support structures,[10,11] with due consideration of the requirement for manufacturing optimization if ever these structures are to be mass-produced.

OWTs are subject to more significant dynamic structural responses than conventional jacket platforms utilized on the oil and gas industry as a result of the effects of wind load and turbine behaviours. The fatigue load levels as well as the number of cycles to be accounted for are especially of note. The fatigue damage contribution for the multiplanar welded tubular joint from wind load effects can be high (exceeding 60% of the total), and the number of hot spot stress cycles associated with wind and wave loads in a year can exceed 7×10^7. Hence, the fatigue performance of members is a design driving criterion for numerous structural details of OWT foundations.[6,12]

Structural design and analysis have initially been based on deterministic methods. However, it is potentially advantageous that probabilistic based methods could be employed due to the uncertainties in loads, strengths and structural modelling. As a fundamental design driver, a structure is expected to perform satisfactorily within a design life. This means for OWTs that it must fulfil specific functional requirements and does not become unsafe over, generally, at least 25 years.[13] Several studies[1,3,12,14–18] have already applied the structural reliability methodology for the safety assessment of offshore structures. However, most reliability methods assume that the system is time-invariant. In practical OWT instances, due to the degradation brought by corrosion and fatigue, as well as fluctuating loads in time, the system becomes time-variant.

Models used to determine the response of support structures for OWTs can be either one-dimensional (1-D) beam models or three-dimensional (3-D) finite element analysis (FEA) models. The 3-D FEA models are generally more advantageous because they are able to investigate detailed stress distributions and capture structural responses more accurately. Because of their high fidelity, 3-D FEA models have been extensively applied to model wind turbine structures,[1,3,19–23] and this study therefore adopts the FEA approach to simulate the responses of OWT jacket support structures.

Because OWT jacket foundations are anchored via piles to the soil system, it is crucial to account for soil-structure interaction to adequately capture the response of the structure. A straightforward method to perform soil modelling is to assume equivalent springs to represent soil based stiffness, which is known as the p-y method.[24] However, in this method, the deflection and the modal frequency are underestimated. A more reliable way of carrying out soil modelling is to define 3-D FEA brick elements to achieve precision and reliability in the results.[25,26] Considering its efficacy, 3-D FEA with brick elements is adopted to model the soil in this study.

A most severe form of localized corrosion is pitting corrosion, characterized by the evolution of pits that penetrate the metal, leading to local mass loss. It is considered one of the most crucial degradation mechanisms as cracks are seen to initiate and propagate in structures from these corrosion pits under sustained fatigue loading.[27] According to the literature,[28,29] the analysis of the effect of corrosion on the structural reliability of jacket type offshore structures is a subject open to investigation. There have been very few detailed studies for failures in offshore structures due to pitting characteristics. Cyclic loads of variable amplitude resulting from wind speed variations and wave motion fluctuations referred to as stochastic loads coupled with environments containing chloride jeopardize the structural capability of OWT structures.[29]

To address the above challenges, this study aims to (a) develop a corrosion fatigue model based on pit and crack growth; (b) predict the nucleation/development and growth to critical size of the corrosion pits using data obtained from the literature; (c) predict pit to crack transition and crack propagation using the sequential steps of a high capability tool applying fracture mechanics functions and afterwards building stochastic parametric FEA model; (d) apply surrogate/meta model methods via artificial neural network (ANN) response surface method (RSM) to post-process the data in order to aid in expressing the limit state/performance function in terms of important stochastic variables; and (e) perform structural reliability assessment (SRA) that employs the generated limit state function (LSF) using widely recognized numerical reliability assessment techniques such as first-order reliability method (FORM) and Monte Carlo simulation (MCS).

ANNs are established to be universal function approximators and have found applications in SRA by several researchers.[30–35] The neural structure of the brain has been employed in creating mathematical models defining ANNs. ANNs establish a functional relationship between two

spaces of data during a learning process and replicate that connection during a recall process. The multilayer feed-forward network is the most widely used ANN architecture.[35] According to Cardoso et al,[36] ANNs can approximate highly non-linear functions accurately over the entire domain with very high fidelity. Several studies[32,34] have also been carried out, proving the precision and efficiency of the RSM based on ANN in comparison with the conventional RSMs for reliability assessment. According to Chojaczyk et al,[35] ANN-based reliability assessment methods are robust and efficient alternatives compared with conventional reliability analysis methods for complex structures, especially those requiring training set selection techniques that are advanced.

In Shi and Mahadevan,[37] a comprehensive mechanics-based probabilistic model for pitting corrosion-fatigue life prediction for aluminium alloys by including all stages was presented where an analytical FORM and MCS were implemented with the proposed model. An extensive review that focuses on the recent developments in the methodologies used for predicting pitting corrosion-fatigue lifetime especially pit-to-crack transition was presented in Larrosa et al.[29] In Li and Akid,[38] the pitting corrosion-fatigue behaviour of a medium strength structural steel shaft was studied in seawater. Emphasis was placed on the study of corrosion pit formation and the development of cracks from pits. A model that included the stages of pitting and the pit-to-crack transition was developed in order to predict the fatigue life by quantifying the pitting and crack propagation throughout the fatigue loading. There are several classical pitting corrosion-fatigue models some of which are included in other studies.[38–45] Recent works on structural reliability with respect to fracture where a new methodology for the statistical inference of the equivalent initial flaw size distribution (EIFSD) using dual boundary element method was proposed in other studies. [46,47] To the best of the authors' knowledge, the work presented herein, in this study, is the first of its kind where the SRA of a steel OWT support structure subjected to pitting corrosion-fatigue is performed by applying a new approach to damage tolerance modelling methodology. In this study, in order to accurately predict the pit-to-crack transition behaviour, a stochastic parametric FEA model was built and incorporated with FORM for approximating time-variant reliability levels of the structure via ANN. The novelty of this paper is in the application of the reliability analysis together with a stochastic approach where the short and long crack models are combined to determine the damage tolerance design of OWT structure. Apart from accounting for the uncertainties involved in modelling pitting corrosion-fatigue mechanisms, this study incorporates the responses of the structure to environmental loads such as due to wind, wave and current as well as due to soil-structure interaction.

The stochastic expansion consists of the intrusive and non-intrusive formulations. An intrusive formulation is the one whereby the representation of uncertainty is expressed explicitly within the analysis of the system. Practically, this refers to methods that use Karhunen–Leove expansion (K-L) and polynomial chaos expansion (PCE) to directly modify the stiffness matrix of a FEA procedure, such as spectral stochastic FEM (SSFEM) and stochastic Galerkin FEM. On the other hand, non-intrusive formulations, such as stochastic RSMs,[6,17,48] represent uncertainties in a nonexplicit way and treat the analysis code as a 'black box' without requiring access to the source code. Surrogate models, also referred to as meta-models or response surface models (e.g. based on the ANN, Kriging and support vector machines), are used for time-consuming implicit LSFs (i.e. which will require the use of FEA) such as obtained in complex frame type structures as adopted herein. In this study, a non-intrusive SRA formulation is proposed for the probabilistic evaluation of the structure considering pitting corrosion-fatigue mechanism in the application of the damage tolerance model method. It involves the combination of high capability tools: Separating Morphing and Adaptive Remeshing Technology (SMART) fracture© and DesignXplorer© as packaged in ANSYS, with FORM through ANN in the non-intrusive formulation.

This paper is organized as follows. Section 2 presents the theoretical background where the SMART crack growth analysis package in ANSYS workbench as well as the fracture mechanics analysis of planar flaws and corrosion fatigue modelling are discussed. Section 3 discusses the methodology adopted in the present study, where global elements to be considered when designing a typical OWT support structure are presented, an OWT support structure subjected to pitting corrosion fatigue at critical joint is reviewed and then the implementation method of SRA taking into account stochastic variables is discussed. Section 4 presents the results obtained from the analysis and a comprehensive discussion is provided on the mesh optimization, validation of the FEA-based fracture mechanics model results, pitting corrosion-fatigue SRA results and global sensitivity analysis results, and finally, Section 5 presents the conclusions drawn from the present study.

2 | RESEARCH BACKGROUND

2.1 | SMART© crack growth analysis

Fracture simulation has relied on two models: traditional cohesive zone modelling (CZM) and, more recently, the extended finite element method (XFEM). CZM is commonly applied to the simulation of de-bonding between two surfaces attached adhesively. CZM is ideal for simulating composites, but it is generally not suitable for simulating the crack growth in the bulk of a material.[49]

The XFEM is better for internal crack calculations. Introduced into ANSYS toolkit, XFEM eliminates the need for remeshing crack tip regions. Instead, it defines an extended finite element enrichment area around the crack tip and in regions where it is plausible that the crack tip might grow. XFEM splits the special volume elements in the enrichment zone from the centre of the element. In this way, it creates a finer mesh by splitting existing cells instead of remeshing. However, the enrichment regions in XFEM are very computationally expensive and as the enrichment area increases, the simulation slows down. Hence, XFEM is not easy to scale up to large projects, which led to the development of the SMART© crack growth tool.

SMART© relies on the unstructured mesh method (UMM) process. SMART© updates the mesh from crack-geometry changes due to crack growth automatically at each solution step. It is a new feature introduced in ANSYS R19. Instead of using the enrichment technique, it uses a localized remesh function as the crack grows. Unlike the XFEM, SMART© can be scaled up for larger projects because remeshing is limited to a small area around the crack tip at each iteration. An advantage is that in this technique, there is no need to develop new elements, and standard elements already included in mechanical, that is, the conventional solid 187, 186 and so forth can still be used. The software also enables engineers to enter alternative crack growth laws as these emerge from new research about the particular material being modelled.

The following important characteristics of the SMART© crack-growth method pertain to its use: (1) it only applies to 3-D Mode 1 dominant crack growth. (2) It only supports linear elastic isotropic materials. (3) It is being developed for the solid 187 (quadratic tetrahedral element) only. This is because the tetrahedral element can model any geometry, unlike the hex element, where there could be difficulty in some cases. It currently ignores the large-deflection and finite-rotation effects, crack tip plasticity effects, and crack-tip closure or compression effects. The fracture criteria for static crack growth include critical stress-intensity factor K_I and J-integral J. The fatigue crack growth is based on Paris' law.[50]

2.2 | Fracture mechanics analysis of planar flaws

In BS 7910,[51] two methods both based on fracture mechanics crack analysis under fatigue loading that include a general procedure and a simplified procedure associated with S-N curves have been outlined for the assessment of planar flaws. The methods evaluate the fatigue life by the integration of the crack growth law. The general procedure allows accurate expressions for cyclic stress intensity factor to be used as well as specific data for fatigue crack growth. The quality category procedure implies the use of fracture mechanics calculation results that have been already conducted and depicted graphically.

It is common in a fracture mechanics assessment to employ conservative estimates of the various parameters required. However, an alternative approach is to employ reliability methods to account for the parameter uncertainties. In the fracture mechanics approach, an assumption is made that a flaw can be considered as a crack with a sharp tip which propagates according to the law associated with crack growth rate, da/dN and stress intensity factor range, ΔK, for the flaw containing material. The crack growth law is generated experimentally. It is normally observed that the overall relationship between da/dN and ΔK is a sigmoid curve in a $log(da/dN)$ versus $log(\Delta K)$ plot. It is reasonable to assume a linear relationship (i.e. the Paris' law) at the central portion of the plot; or for greater accuracy, the data are represented by two or more straight lines. The rate of growth rate falls rapidly at low values of ΔK such that there is insignificant crack growth below a threshold stress intensity factor range, ΔK_0. When the maximum stress intensity factor K_{max}, at high values of ΔK, approaches the critical stress intensity factor for static load failure, K_c, there is a rapid acceleration in the rate of crack growth. However, it is usually assumed that the central portion is applicable for all ΔK values (from ΔK_0 up to failure). The Paris' law equation is given by the following equation[50,51]:

$$\frac{da}{dN} = C(\Delta K)^m \tag{1}$$

where C and m are material coefficients and also depend on environmental effects. For $\Delta K < \Delta K_0$, da/dN is assumed to be zero. The stress intensity factor range, ΔK, is a function of geometry factor, Y, stress range, $\Delta\sigma$, and instantaneous crack size, a, and is calculated from the following equation:

$$\Delta K = Y(\Delta\sigma)\sqrt{(\pi a)} \tag{2}$$

The overall life is calculated by substituting Equation 2 into Equation 1 and integrating the following equation:

$$\int_{a_i}^{a_f} \frac{da}{Y^m(\pi a)^{m/2}} = C(\Delta\sigma)^m N \tag{3}$$

The acceptability of a crack of initial size a_i then depends on whether the calculated cyclic life, N, is greater or less than the required life. If the initial crack size a_i and final crack size a_f are known, the number of cycles to failure can be obtained through integrating Equation 3:

$$N_f = \frac{2}{C\Delta\sigma^m Y^m \pi^{\frac{m}{2}}(2-m)}\left[a_f^{1-\frac{m}{2}} - a_i^{1-\frac{m}{2}}\right] \tag{4}$$

Based on the assessment procedures for tubular joints in offshore structures (see BS 7910), the stress analysis and fatigue assessment can be performed as follows.

In the stress analysis, it is important to acquire the forces and moments in the members of the assessed regions under critical loading conditions, as a result of the structural analysis of the entire frame. These include the axial force, in-plane and out-of-plane bending moments. Both ranges of maximum as well as fatigue load are required. The current literature identifies two types of stress analysis: global and local. In order to evaluate the stress spectrum associated with the wave loading at the location of a flaw, the global FEA of the entire structure is conducted. A histogram of the wave height against the number of occurrences is constructed using the wave exceedance curve. The global structural analysis is used to determine the stress range corresponding to each wave height. The latter gives the loading at the nominal brace as a result of the fatigue action as well as loading from storm waves. Hence, stress ranges corresponding to the axial, in-plane bending and out-of-plane bending brace ($\Delta\sigma_{AX}$, $\Delta\sigma_{IPB}$ and $\Delta\sigma_{OPB}$, respectively) are calculated for each wave height.

On the other hand, local stress analysis aims to find the stress range variation around the periphery of the joint as well as the evaluation of the stress range histograms for at least eight equally spaced positions, including the saddle and crown locations. Note that bending loads and nominal brace axial resulting from the chord reaction generates stress ranges at the local joint. The tubular walls local deformation leads to the development of high secondary bending stresses. This results in through-thickness stress gradients and high-stress concentrations at the intersection of the brace/chord.

In this paper, the global and local structural analysis methods are adopted from BS 7910[51], as part of the theoretical analysis. For the fatigue assessment, the damage variation at the periphery of the joint should be evaluated, and the stress range histogram for the maximum damage in the selected crack region. The application of the stress range histogram is then performed on a block by block basis.

Corrosion pits at different locations of a joint and interaction between the pits necessarily results in variation of localized stress near a crack and then have critical effect on calculation of the crack size. According to BS 7910,[51] multiple flaws in close proximity can lead to an interaction and to more severe effects than single flaws alone. Also, according to the same standard, it is not necessary to apply flaw interaction criteria for fatigue assessment. However, if there is any uncertainty as to whether flaws are separate they should be combined or specific calculations carried out. The effective dimension after interaction as prescribed in BS 7910[51] is $a = \max. \{a_1, a_2\}$ where a_i is the depth of a coplanar surface flaw that has been adopted in this study.

2.3 | Modelling of corrosion fatigue

The process of corrosion fatigue is synergistic, occurring as a result of electrochemical, microstructural and mechanical loading interactions. The process includes pit formation, pit growth, crack nucleation from pits and crack propagation. The proportions of the time spent/cycles in each of these systems are dependent on the material/environment system, stress magnitude and applied load frequency. The modelling approach for corrosion fatigue process found in several studies [26,37–40] is simplified into the three main regimes: pit growth N_{pit}, small crack growth N_s and long crack growth N_l. The total life due to fatigue (N) can be expressed as the summation of each of the individual stages.[38] Thus,

$$N = N_{pit} + N_s + N_l \tag{5}$$

2.3.1 | Assumptions

The following assumptions are made for this study[38,40,51]:

1. The failure cracks nucleated in the largest corrosion pits.
2. The corrosion-fatigue process is composed of two stages: crack initiation composed of pit nucleation and pit growth and corrosion-fatigue crack propagation.
3. There is a critical pit size for the transition from crack pit initiation to crack growth
4. Both the pitting growth and fatigue crack nucleation from pits control the corrosion-fatigue initiation life.
5. The critical pit is assumed as a semi-circular surface crack (hemispherical pits)

2.3.2 | Corrosion pit growth law (N$_{pit}$)

According to several studies,[29,38,40] it is common to apply two methods in determining the pit growth depth, as follows:

a. Exponential relation to t (Exponential law)

In Sriraman and Pidaparti,[42,43] it was revealed that for a given corrosion pit, the depth a_p at time t can be defined by the following equation:

$$a_p = A.\left(\frac{t}{t_f}\right)^B \tag{6}$$

where t_f represents the time which corresponds to the number of cycles to failure, and A and B are respectively coefficient and exponent. Assuming a constant test frequency f(Hz), then $t = \frac{N}{f}$, and a_p can be defined by

$$a_p = A.\left(\frac{N_{pit}}{N_f}\right)^B \tag{7}$$

The parameters A and B that are pit growth-dependent can be determined by interpolating the test data (for more see Wu[44]).

b. Faraday's law

The application of the Faraday's law has been in defining the pit growth law, which has been validated against experimental results.[39,42,43] The corrosion pit depth a_p in a material is proportional to the cube root of t and is expressed by the following equation[38]:

$$a_p = \left(\frac{3M.I_p}{2\pi.n.F.\rho}\right)^{\frac{1}{3}}(t)^{\frac{1}{3}} \tag{8}$$

where I_p denotes the pit current (mA) that can be obtained from Saha[52]; M refers to the material's atomic mass (kg/mol); ρ represents density (kg/m^3); F denotes Faraday's constant (C/mol) and n represents the number of released electrons during the metal corrosion. The pit current I_p can be calculated from

$$I_p = I_{po}.\exp\left(-\frac{\Delta H}{RT}\right) \tag{9}$$

where I_{po} denotes the pit current coefficient (C/s); H denotes the activation energy (enthalpy change, J/mol); R denotes the universal gas constant (J/mol K) and T denotes the absolute temperature (K). For the surface of a component consisting of hemispherical pits assumed similar to an infinite plate containing the 2D semi-circular surface flaw, the stress intensity factor range ΔK can be determined for a pitted surface from the following equation[40]:

$$\Delta K = \left(\frac{2.2}{\pi}\right)K_t.\Delta\sigma.\sqrt{\pi.a_{pc}} \tag{10}$$

$$a_{pc} = \pi\left(\frac{\Delta K_{th}}{4.4K_t.\sigma_a}\right)^2 \tag{11}$$

$$N_{pit} = \left(\frac{a_{pc}}{A}\right)^{1/B}.\left(\frac{10^{9.19}}{e^{0.036\sigma_a}}\right) \tag{12}$$

where a_{pc} represents the critical pit size necessary for pit to crack transition (μm); K_t represents the stress concentration factor (SCF) that is derived from the curves in Cerit et al[53]. The number of cycles to crack initiation N_{pit} can be determined by substituting Equation 11 and the stress and fatigue life relationship (i.e. seawater environment S-N data) into Equation 7.

2.3.3 | Corrosion fatigue 'small crack' life (N_s)

It has proven troublesome to establish an explicit formula describing the growth of short cracks, despite the high amount of research that has been conducted in this area, particularly for corrosive environments. According to some authors, the following empirical formula that is similar in form to the Paris' law can be employed,[42,45] which has been validated with test data.[38]

$$\frac{da}{dN_s} = C_s(\Delta K)^{m_s} \tag{13}$$

C_s and m_s can be determined by fitting the experimental data.[29,38] The notional concept of stress intensity factor can be employed, when a suitable parameter for describing the growth of small cracks under corrosion fatigue conditions is unavailable. Solving Equation 13 within the limits a_{pc} to a_{tr}, the consumed number of cycles during the stage of small crack growth can be calculated from the following equation:

$$N_s = \int_{a_{pc}}^{a_{tr}} \frac{1}{C_s(\Delta K)^{m_s}}da \tag{14}$$

where a_{tr} denotes the crack length for small to long crack transition.

2.3.4 | Corrosion fatigue long crack life (N_l)

The stage for long crack growth life can be ascertained using the Paris' law. Therefore,

$$\frac{da}{dN_l} = C_l (\Delta K)^{m_l} \tag{15}$$

where C_l and m_l can be determined from the experimental data.[38,53,54] Solving Equation 15 using the limits a_{tr} to a_f (where a_f is computed from K_{IC}), the long crack growth life stage can be determined from

$$N_l = \int_{a_{tr}}^{a_f} \frac{1}{C_l (\Delta K)^{m_l}} \, da \tag{16}$$

2.3.5 | K-T diagram in air and artificial seawater

According to the linear elastic fracture mechanics (LEFM) approach, for crack propagation to take place the defect must be at threshold size. Hence, crack depths below this critical size will not grow on smooth surfaces. However, LEFM does not apply in cases where defects are small as a result of localised plasticity connected with such cracks. A Kitagawa–Takahashi (K-T) diagram that associates the threshold ΔK_{th} and the fatigue limit to the fatigue crack size has been established, to take into account the two approaches of pre-existing cracks (LEFM) and nominally defect-free samples (S-N curves).

According to several studies, it was revealed that short crack growth rate exceeds the corresponding long crack growth rate (for an 'equivalent' ΔK value) and that below the threshold ΔK_{th} short cracks growth occurs. Hence, taking short cracks into consideration, where a_0 is assumed to represent the length of crack below which the fatigue limit ceases to be independent on crack size, Equation 17, then the fatigue stress range variation can be defined as a function of crack size, Equation 18.

$$a_0 = \left(\frac{1}{\pi} \right) \left(\frac{\Delta K_{th}}{Y \Delta \sigma_e} \right)^2 \tag{17}$$

$$\Delta K_{th} = Y \Delta \sigma_e \sqrt{\pi (a + a_0)} \tag{18}$$

where Y represents the shape factor and $\Delta \sigma_e$ represents the fatigue limit range (two times of the fatigue limit). Figure 1 depicts a comparison of the K-T diagrams in air and artificial seawater, according to Li and Akid.[38] The A–B region, is defined as the microstructural short crack (MSC) regime while B–C as the physically small crack regime (PSC).
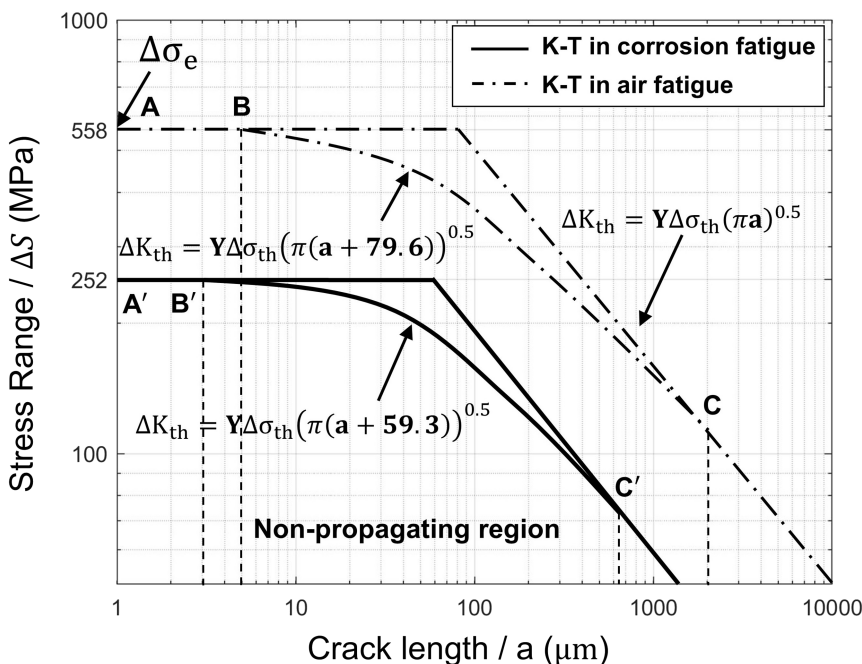

FIGURE 1 The Kitagawa–Takahashi (K-T) diagrams for air and artificial seawater environments. Source: Li and Akid[38]

3 | METHODOLOGY

3.1 | Design considerations for OWT support structures

3.1.1 | Parametric modelling of OWT jacket support structures: geometry, materials, structural components and soil profile

The reference case used for this analysis consists of a baseline 10-MW NREL wind turbine, connected to an 88.4 m tower, a transition piece (TP) and is sustained by a jacket foundation. The jacket is 66 m vertical height, and the piles are embedded 42 m into the soil and submerged 50 m into the ocean. The piles are to be driven through the legs and thus feature a batter angle. The TP is 7 m in length and joins together the jacket and the tower.[10,11] The OWT support structure was modelled using ANSYS, which is a widely used FEA software[6] (see Table 1 and Figure 3A).

The jacket, TP, piles and tower are made of steel S355 with a density of 8,500 kg/m^3, Young's modulus of 210 GPa, and a Poisson's ratio of 0.3.[10,11] Aside from the OWT support structure, the soil-structure interaction is also an important design factor of the structural response model of the pile-jacket-tower assembly. Although the soil-structure interaction aspect is often neglected in OWT support structures modelling,[55] it is included in this study for improved accuracy of the results. For this study, the soil profile is modelled as six layers of sand, corresponding to that of a deepwater site located off the coast of Netherlands designated as the K-13 deep-water site. Table 2 gives the soil profile parameters used in the simulations, which are based on site measurements. A cylindrical shape (D = 140 m, H = 50 m) is assumed with six different strata to model the soil system in ANSYS (see Table 2). The Drucker–Prager strength linear model is adopted to model the soil material.[56] This model is employed in calculating each soil strata yield stress. The soil's yield strength, σ_{ys}, based on the Drucker–Prager model, can be expressed as

TABLE 1 Baseline 10 MW support structure parameters[6,9,10,48,49]

Parameter	Value
Deck height above MSL (m)	16
Water depth (m)	50
Leg OD (m)	1.74
Leg wall thickness (m)	0.030
Number of bays	4
Jacket batter	8.47
Height of TP (m)	7
Number of legs	4
Pile OD (m)	1.59
Pile wall thickness (m)	0.037
Mud brace OD (m)	0.762
Mud brace wall thickness (m)	0.017
x-brace outer diameter (m)	0.61
x-brace wall thickness (m)	0.016
RNA mass (kg)	1 072 000
Tower length (m)	88.4
Tower-top OD (m)	3.85
Tower-top thickness (m)	0.03
Tower-base OD (m)	7
Tower-base thickness (m)	0.055
Thrust associated with rated power ultimate load (UL) case (kN)	1700
Maximum rotor thrust taking into account dynamic amplification UL case (kN)	3400
Thrust fatigue load (FL) case (kN)	203
Torsional moment UL case (kN-m)	7876
Torsional moment FL case (kN-m)	3483
Tilting moment UL case (kN-m)	38 567
Tilting moment FL case (kN-m)	3687

Abbreviations: MSL, mean sea level; OD, outside diameter; RNA, rotor nacelle assembly; TP, transition piece.
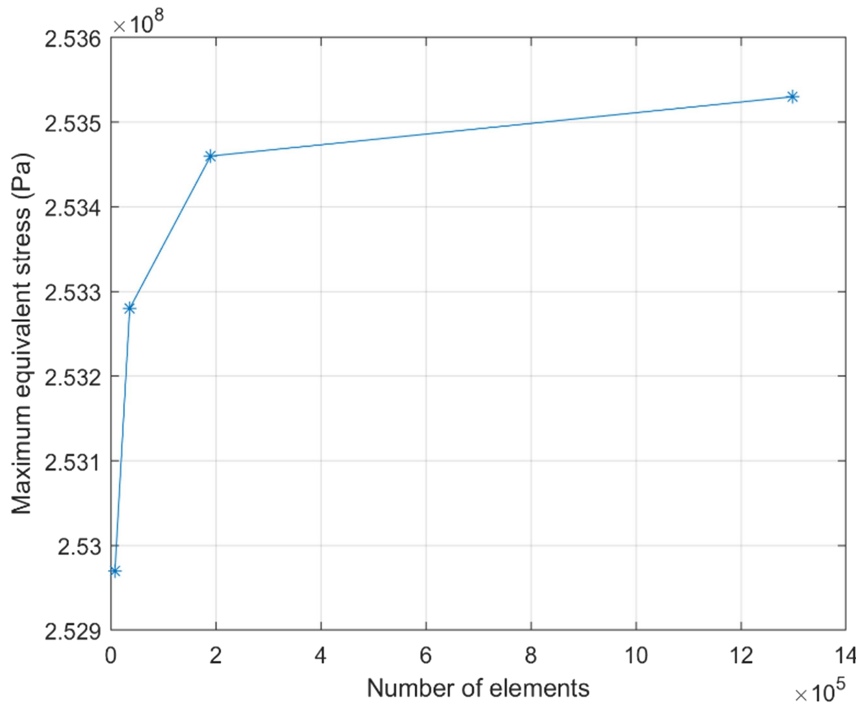
TABLE 2 K-13 deep-water site's soil profile[6,10]

Depth below seabed (m)	Unit weight N/m^3	Friction angle (°)	Shear strength (N/m^2)	Young's modulus (MPa)
0–3	10 000	36	60 000	30
3–5	10 000	33	60 000	30
5–7	10 000	26	60 000	50
7–10	10 000	37	60 000	50
10–15	10 000	35	60 000	50
15–50	10 000	37.5	60 000	80

$$\sigma_{y,s} = \frac{6c\,\cos\phi}{\sqrt{3}(3 - \sin\phi)} \tag{19}$$

Here, ϕ denotes the internal friction angle and c denotes the cohesion value. Between the soil and the pile, the associated coefficient of friction C_f can be expressed as[25]

$$C_f = \tan\left(\frac{2}{3}\phi\right) \tag{20}$$

3.1.2 | Mesh sensitivity analysis

A mesh sensitivity analysis was performed in order to optimize the element size and thus enhance the accuracy of results. The results are presented in Table 3 and Figure 2. Based on the mesh sensitivity analysis, convergence of the Von-Mises (equivalent) stress was achieved at the soil element size of 2 m and support structure element size at 0.5 m, corresponding to a number of mesh totalling 190 222.

TABLE 3 Mesh sensitivity[6]

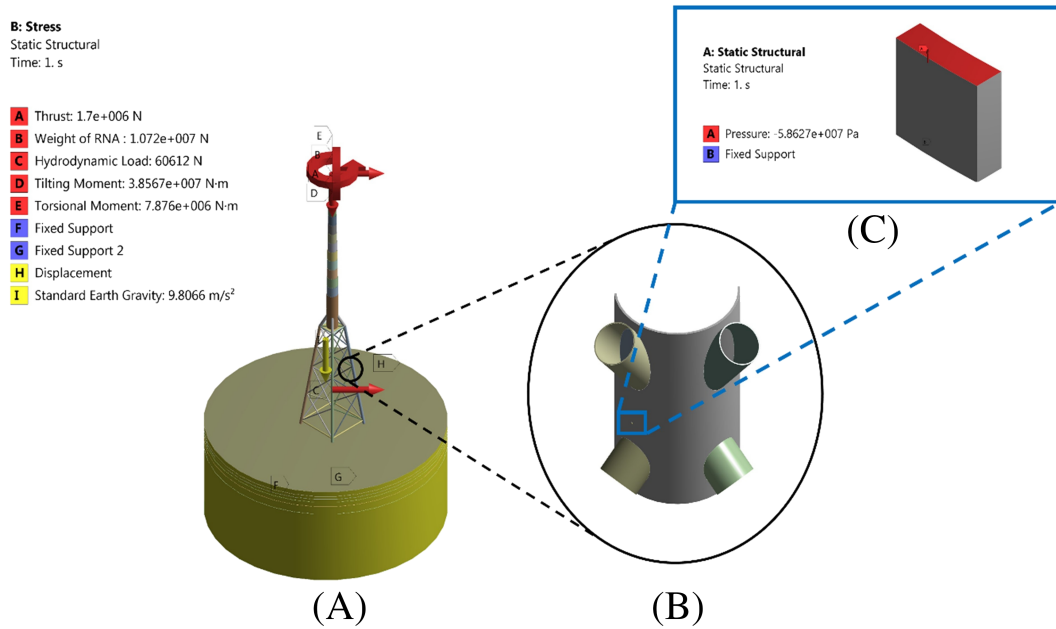| Soil element size (m)	Jacket structure element size (m)	Number of elements	Maximum Von-Mises stress (Pa)
8	2	8047	2.5297E + 08
4	1	36 164	2.5328E + 08
2	0.5	190 222	2.5346E + 08
1	0.25	1 298 092	2.5353E + 08

FIGURE 3 The 3-D structural model: (A) with applied loads and boundary conditions (BC) on a global scale[6]; (B) half of the critical joint of the support substructure showing hemispherical pit; (C) curved plate with applied stress and BC [Colour figure can be viewed at wileyonlinelibrary.com]

3.1.3 | Validation

This model has been validated by comparing the results of the modal analysis deflection in static analysis for the support structure against data from the reference OWT. Results of the modal analysis and deflection can be seen in Tables 4 and 5, respectively, where it can be appreciated that the first eigen-frequency of the model is within the range that typically represents the 3P frequency of the rotor. Moreover, the eigen-frequency is 0.21346, which represents 0.12% of the relative difference from the one obtained in Damiani et al [11] and Damiani.[57] Also, the deflection at the RNA elevation and tower base is 1.236 m and 1.6085×10^{-1}, which represents −0.46% and −3.44% of the relative difference from the one obtained in Damiani et al.[11] These differences are considered to be acceptable.

3.1.4 | Calculation of loads on OWT support structures

In this study, the environmental conditions of the design approach are defined as the normal operating conditions for the fatigue limit state (FLS; see Section 3.3.1). Wave, wind and current loads are calculated manually and then incorporated in the parametric FEA model.

TABLE 4 Comparison of the support structure mode frequencies with reference values[6]

Mode frequencies (Hz)	Present	References[11, 57]	Difference (%)
First side-to-side bending	0.21346	0.21320	0.12
First fore-aft bending	0.22297	0.21629	2.99
Second side-side bending	1.1602	1.0313	11.11
Second fore-aft bending	1.5292	1.6561	−8.29

TABLE 5 Static deformation of the baseline 10 MW wind turbine jacket[6]

Load case	Displacement at RNA			Displacement at the tower base		
Mass/Thrust	Present	Ref.[11]	Diff (%)	Present	Ref.[11]	Diff (%)
RNA/3.4 MN	1.263 m	1.2688	−0.46	1.6085×10^{-1}	1.6639×10^{-1}	−3.44

Abbreviation: RNA, rotor nacelle assembly.

The normal wind climate conditions considered in this study are assumed to be cyclic structural loading conditions. These are calculated according to IEC 61400-1,[58] as follows:

$$V(h) = V_{ref} \frac{\ln\left(\frac{h}{z_0}\right)}{\ln\left(\frac{h_{ref}}{z_0}\right)} \tag{21}$$

where z_0 is the roughness coefficient (see Det Norske Veritas [DNV][59]). After generating the wind speed profile, the horizontal force acting on the tower, TP and nacelle, can be calculated as

$$F_x = \frac{1}{2} C_D \rho_e (V_{max})^2 A \cos\alpha \tag{22}$$

where C_D is the cylindrical drag coefficient (for the tower and TP) and plate drag coefficient (for the nacelle), A is the area being pushed by the wind and α is the inclination angle of the wind with the horizontal axis. Blades are not accounted for in this study.

For the calculation the wave forces, Morrison's equation is used. The equation is composed of two terms, namely, the inertia, as identified by the inertia coefficient C_m, and the drag, as identified by the drag coefficient C_d.[60] Morrison's equation is given by

$$F = F_d + F_m = \frac{1}{2} \rho_w C_d D |u_x| u_x + \rho_w C_m \frac{\pi D^2}{4} \frac{dU}{dt} \tag{23}$$

where U is the undisturbed fluid velocity, $\frac{dU}{dt}$ is the acceleration of the fluid, ρ_w is the water density, and D is the diameter of the cylinder. From the wave profile data depicted in Table 6, Stokes third-order wave theory can be used to model wave characteristics and behaviours. Stokes wave theory is the most widely employed method applied in the offshore structural analysis because of its precision in predicting the wave kinematic properties.

Environmental loads, including tidal currents and wind-driven currents, do not pose significant hazards to integrity of structures in shallow water. However, they can contribute to other significant excitations such as those generated by the wind and waves. The current speed ($v(z)$) can be used to represent the tidal current profile at distance z, from still water level. The current speed varies exponentially from the current at the level of still water v_0 through the distance to the topwater column z. This is given by

$$v(z) = v_0 \left(\frac{h+z}{h}\right)^{\frac{1}{7}} \text{ for } z \geq 0 \tag{24}$$

where h is the depth of water. The extreme tidal current occurs approximately at mean water level, with zero tidal currents at high and low tide. Once the tidal current profile is determined, a constant over depth current will be assumed. Wind-driven currents are as a result of shear forces imposed on the water surface due to wind and are, hence, likely to have the same orientation in a similar direction with the wind. The sea surface wind-driven current can be approximated according to IEC61400-3, as

$$U_{wind} \approx 0.01 U_{1h,10min} \tag{25}$$

where $U_{1h,10min}$ is the hourly mean at 10 m height.

TABLE 6 Water levels and wave data of interest for the K-13 deepwater site[6]

Parameter	Value
Lowest astronomical tide, LAT (m)	−1.06
Tidal range, Δz_{tide} (m)	2.22
Storm surge, Δz_{surge} (m)	2.13
Air gap, Δz_{air} (m)	1.5
Significant wave height, H_s (m)	9.4
Maximum 50-year wave height, $H_{50,max}$ (m)	17.48
Maximum wave period range, T_{50} (s)	10.8–14
Max. wave height above still water for deck height calculation, ξ_w (m)	11.36

Hydrostatic pressure is the pressure of the water column the submerged jacket parts are subjected to. This can be evaluated by using a control volume analysis of an infinitesimally small cube of fluid by making a simplified assumption having constant gravity as well as density through depth. Therefore,

$$p(z) - p(z_0) = \frac{1}{A} \int_{z_0}^{z} dz' \int \int^{\rho} (z')g(z')dA = \int_{z_0}^{z} dz' \rho(z')g(z') = \rho gh \tag{26}$$

where $p(z)$ is the pressure at a given height z, $p(z_0)$ is the pressure at z_0, which is the top of the water column, Therefore, $p(z_0) = P_{atm}$, ρ is the water density (kg/m^3), g is the gravity (m/s^2), $h = (z − z_0)$ is the height of the liquid column between the test volume and the zero reference point of the pressure.

The nacelle and rotor are modelled in the FEA as concentrated or distributed masses. This means that the hub and blades are not part of the parametric model. According to Martinez-Luengo,[55] it is not necessary to model the blades because, apart from the added mass applied to the top of the tower, the impact of the parked and feathered blades on the eigen-frequency of OWTs is not significant. The rotor nacelle assembly (RNA) mass is 1072 t.

The structural integrity of the support structure is checked according to DNV-OS-J101, which is the most widely used standard in the design of OWTs. According to this standard, four limit states have to be considered in the design: ultimate limit state (ULS), FLS, accidental limit state (ALS) and serviceability limit state (SLS). This study focuses on FLS because according to several studies fatigue is the design driving criteria for offshore structural members.[3,12] For a detailed description of the ULS and FLS, the readers may refer to other studies.[3,6,18,50]

3.2 | OWT support structure subjected to pitting corrosion-fatigue

3.2.1 | FEA model applying experimental procedure for validation

The material sample used is carbon steel material with maximum tensile strength of 610 MPa, yield strength of 375 MPa and elongation of 18%.[38] A dog-bone-shaped sample is modelled in ANSYS environment employing the 4-point rotating bending fatigue test. The sample is prepitted in the centre section of the gauge length with the pit having diameter and depth of 0.9 and 0.1 mm respectively, and a pit aspect ratio of around 0.11. In-air and corrosion-fatigue tests were conducted under load control at $R = −1$. Further details of the experimental data that were used and results to be compared for validation can be found in Li and Akid.[38] Details of the rotating bending test set-up as adapted for this study can be found in Hassan and Liu.[61]

3.2.2 | Parametric FEA

The jacket configuration, the sources of loads and a parametric FEA model of the 3-D space frame, tower and pile assembly (as shown in Figure 3A) have been presented in this section. The present study is a continuation of the analysis been carried out in Shittu et al.[6] An ANN architecture is used in obtaining an expression to relate the input parameters with the output maximum stress range, which will be used later in this study. The parametric FEA, which will be used in this study, is presented in as follows:

From the parametric FEA model explained earlier in this subsection, the critical joint is assessed by subjecting it to pitting corrosion, and the result is shown in Figure 3B. Because the pit size is very small, 223μm, a model of a curved plate containing the crack is considered around the vicinity of the crack, in order to limit computational time/cost to practical levels.

The FEA model built in Shittu et al[6] is used to find the equivalent stress at the vicinity of the pit, and the result is applied to the plate (see Figure 3C). The equivalent stress acting on the plate as modelled is then found to be 58.63 MPa.

A crucial step in assessment of the model to be applied for FEA is the mesh generation. The ANSYS software package provides a powerful and reliable structure mesh generator capable of developing a mesh that is consistent in all of the structure with the minimal computational requirement.

3.3 | SRA of the OWT support structure

In this section, the structural reliability of the OWT support structure subjected to pitting corrosion fatigue is assessed based on the damage tolerance approach considering FLS according to DNV-OS-J101.[59] The SRA is carried out in two phases: the pit growth regime and the pit to crack transition regimes. Equation 11 is used to determine the critical pit depth necessary for pit-to-crack transition, establishing a_{pc} = 223μm. This is

also confirmed using the T-K diagram in Figure 1 herein and from Li and Akid.[38] Then, Equation 7 is used to calculate the time in years for the crack to reach critical size, establishing t = 9 years.

The fully parametric FEA model presented in Section 3 is used to perform FEA modelling taking into account of stochastic variables. The results are then post-processed using a non-intrusive formulation as developed in this study.

3.3.1 | Fatigue limit state

OWT jackets are subjected to significant cyclic loads induced by wind and wave, and therefore, their design is generally dominated by FLS. The FLS can be assessed by using two types of methods, that is, S-N curve method and fracture mechanics method. According to the S-N curve method, the number of loading cycles to failure, N, can be obtained by[6]

$$\log N = A - m \log \Delta S \tag{27}$$

where A and m are the intercept and the slope of the S-N curve on the log–log plot, respectively, and ΔS is the stress range. The two parameters in Equation 27, that is, intercept A and slope m are generally given by design standards, for example, DNVGL-ST-0126. The performance function of fatigue reliability assessment based on the S-N curve method can be expressed as[1,62]

$$g_{f,SN} = \log N - \log N_t \tag{28}$$

where subscripts f and SN denote the FLS and S-N curve method, respectively; N is the number of loading cycles to failure as given by Equation 27, N_t is the number of loading cycles expected during the given design life. N_t can be estimated based on rated rotor speed n_{rated} and availability η_a (98.5%) on the selected location.[20,63] Thus, considering a lifetime requirement of 20 years, the number of cycles is equal to

$$N_t = \eta_a \cdot n_{rated} \times (20[\text{year}] \times 365[\text{day/year}] \times 24[\text{h/day}] \times 60[\text{min/h}]). \tag{29}$$

Compared with the S-N curve method, the fracture mechanics method is more detailed and involves evaluating crack growth. The performance function for fatigue reliability analysis based on LEFM is given by

$$g_{f,FM} = \int_{a_o}^{a_c} \frac{1}{Y(a)^m \left(\sqrt{\pi a}\right)^m} da - C \Delta S^m (N(t) - N_o) \tag{30}$$

where subscript f and FM denote the FLS and fracture mechanics method, respectively; a_o is the initial crack depth (or the crack depth at time t_0); a_c is the critical crack depth; Y(a) is the geometry correction factor, which is a function of crack depth a; m and C are material constants; $N(t)$ is the total number of stress cycles in the time period $[t_0, t]$; and N_o is the initial number of stress cycles.

3.3.2 | Stochastic variables and FEA

The stochastic variables considered in this study are presented in Tables 7, 8, and 9 for the two crack propagation regimes. Two stochastic variables were considered for the pit growth regime, and five variables considered for the crack propagation regimes, for each of the two cases. The coefficient of variation (COV) of all stochastic variables was assumed to be 0.05, except for inputs to the first ANN which were assumed to be 0.1.[37,64–66] Eight stochastic variables were considered for the first ANN, including thrust force, tilting moment, torsional moment, weight of RNA, hydrodynamic load and three young modulus at three soil strata. The total hydrodynamic load is considered differently, based on its dependence on the wave height, wave period and current speed. To find the peak hydrodynamic force acting on the system, a Weibull distribution is applied to the significant wave height and the current speed, whereas the lognormal distribution is applied to the wave period.[3,59,60] The distribution is then fitted into a Weibull-equivalent distribution. In the presence of observed data, distribution fitting algorithms (such as Akaike information

TABLE 7 Stochastic variables for the pit growth regime

Description	Distribution types	Reference
Critical pit depth	Lognormal	Shi and Mahadevan[37]
Applied stress range	Weibull	Yeter et al[65]

TABLE 8 Stochastic variables for the crack propagation regimes for the SMART© crack growth analysis case

Description	Distribution type	Reference
Young's modulus of steel[b]	Normal	Kolios et al[16]
The major radius of semi-elliptical corrosion pit[b]	Lognormal	Shi and Mahadevan [37]
The minor radius of semi-elliptical corrosion pit[b]	Lognormal	Shi and Mahadevan [37]
Applied stress range[b]	Weibull	Yeter et al [65]
Young's modulus of soils[a]	Normal	Other studies[3,6,64,66]
Thrust force[a]	Normal	Other studies [3,6,64,66]
RNA weight[a]	Normal	Wang and Kolios[3] and Dong et al [12]
Tilting moment[a]	Normal	Wang and Kolios[3] and Dong et al [12]
Torsional moment[a]	Normal	Wang and Kolios[3] and Dong et al [12]
Material constant, C	Lognormal	Shi and Mahadevan [37]
Small crack length	Lognormal	Shi and Mahadevan [37]
Thickness/final crack depth	Lognormal	Shi and Mahadevan [37]

Abbreviation: RNA, rotor nacelle assembly.
[a]Inputs to the first artificial neural network (ANN) architecture.
[b]Inputs to the second ANN architecture.

TABLE 9 Stochastic variables for the crack propagation regimes for the theoretical analysis case

Description	Distribution type	Reference
Pit depth	Lognormal	Shi and Mahadevan [37]
Small crack length	Lognormal	Shi and Mahadevan [37] and Yeter et al [65]
Thickness/final crack depth	Lognormal	Shi and Mahadevan [37] and Yeter et al [65]
Equivalent stress range	Weibull	Shi and Mahadevan [37] and Yeter et al [65]
Material constant, C	Lognormal	Shi and Mahadevan [37] and Yeter et al [65]
Geometry/shape factor	Normal	Shi and Mahadevan [37] and Yeter et al [65]

criterion, Bayesian information criterion and Kolmogorov–Smirnov) are often employed to determine the shape coefficients of the most appropriate statistical distributions.[16]

For the second regime, after defining the stochastic variables, stochastic FEA modelling of the OWT foundation was performed using the FEA model built earlier, as discussed in Section 3.2.2 with the aid of the design of experiments (DoEs) tool in ANSYS. This allows the designation of the various input variables as stochastic, possessing distributions of different types. DoE enhances the design points variation with the output parameters, which are the stress intensity factor range and crack extension.

3.3.3 | SRA using theoretical methods

Having defined the stochastic parameters, for the two methods, in Tables 7, 8 and 9, the performance function is determined by substituting the pit growth regime, small crack regime life and long crack regime life into the FLS equation, that is, substituting Equations 12, 14 and 16 into Equation 30. The resulting performance function can be expressed by Equation 31. Subsequently, the FORM is employed in predicting the time-variant reliability index.

$$g_{f,FM} = \int_{a_{pc}}^{a_{tr}} \frac{1}{Y(a)^{m_s}\left(\sqrt{\pi a}\right)^{m_s}} \, da + \int_{a_{tr}}^{a_f} \frac{1}{Y(a)^{m_l}\left(\sqrt{\pi a}\right)^{m_l}} \, da - C_s \Delta S^{m_s} N(t_s) \, - \, C_l \Delta S^{m_l}\left(N\left(t_{pit} + t_l\right) - N_{pit}\right) \tag{31}$$

3.3.4 | Non-intrusive formulation

A flow chart of the non-intrusive formulation developed for this study is presented in Figure 4. The FEA model built earlier is employed to perform a number of FEA simulations on the plate by adopting the use of the ANSYS DoE package. The DoE used in this study is the Latin hypercube
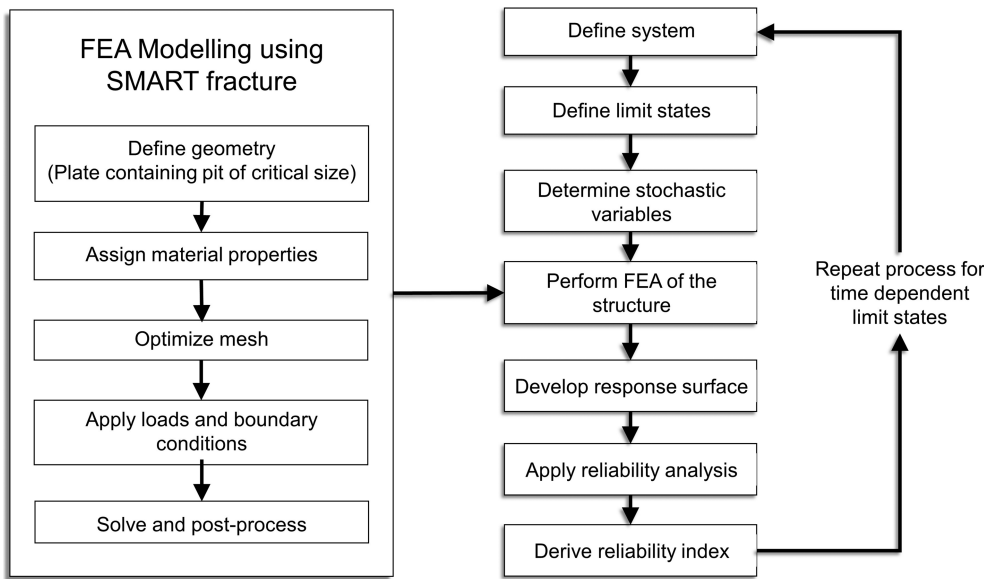
FIGURE 4 Flow chart of non-intrusive formulation. FEA, finite element analysis

sampling design method.[46,47] Further information on the theoretical background on the ANSYS DesignXplorer can be found in other studies.[6,67,68]

Having executed the simulations on the DoE tool packaged in ANSYS, the results are imported into a developed MATLAB algorithm that has been coded for ANN-based response surface modelling (RSM), which is presented in later in this section. In summary, the sequential steps start from defining the system, the corresponding limit state and selection of the parameters to be designated stochastic in the analysis. Next, a series of FEA simulations are executed by changing inputs and recording outputs corresponding to the FLS to map the structural response over the domains of stochastic variables. A suitable method is then employed to estimate the system response and express the output parameters in terms of global inputs. Finally, the reliability index is computed using FORM and MCS. In this instance, the iterative FORM algorithm will be used and compared with MCS for validation of the results. The FORM is widely used because it offers a good balance between accuracy and efficiency for realistic problems. A limitation of the direct simulation method is in its requirement for prohibitively large amount of simulations to estimate the very low values of probability of failure (POF) characterized by complex engineering systems such as offshore structures.[6,46,47]

Two ANNs were trained to relate various stochastic variables for predicting the performance function. The first ANN, named ANN-1, uses Young's modulus of soils, thrust force, RNA weight, hydrodynamic loads and tilting and torsional moments to predict the applied stress range to the structure. The second ANN, named ANN-2, uses Young's modulus of the steel structure, the major and minor radii of corrosion pit and the applied stress range (supplied by ANN-1) to predict the stress intensity factor range, ΔK, and the crack extension, Δa. The latter target variables are then used to compute the LSF. The readers may refer to Table 8 for a summary of the variables involved.

Note that it is possible to use a single ANN that takes the eight stochastic variables as input for predicting the two desired target variables, instead of two separated ANNs. However, having an intermediate predictor for the applied stress range is more advantageous because of the added interpretability of results. The ANNs were trained with data generated from 300 stochastic FEA simulations in ANSYS. The training data set for ANN-1 consists of 300 instances of the eight stochastic variables and one target variable, while that for ANN-2 consists of 300 instances of the four stochastic variables and the two target variables. Both ANN architectures consist of one hidden layer with 10 hidden neurons. The symmetric sigmoid activation function was used in each neuron. The ANNs were trained with 70% of the generated data, validated by the other 15% and tested by the rest. Neural network training was performed using stochastic gradient descent with Bayesian regularization, which were used to obtain the weight values in the ANNs.

The results for training these ANNs are summarized in Table 10, showing high accuracy during both training and testing. This means that the trained ANNs are reliable predictors of the target variables for subsequent structural reliability analysis.

TABLE 10 Training results for the ANNs used in the study

Neural network	Training accuracy[a] (%)	Testing accuracy (%)	Accuracy for all data (%)
ANN-1	99.90	99.71	99.87
ANN-2	99.61	99.58	99.60

Abbreviation: ANN, artificial neural network

[a]Accuracies are given as R^2-values.

Having obtained the performance function from the ANN, the FORM is used to calculate the reliability index β. The procedure for Hasofer and Lind's algorithm is summarized below[69]:

1. Define the performance function for the FLS. This is achieved by substituting the equation expressing the output parameter in terms of the four stochastic input parameters generated via ANN as described earlier in this section into Equation 2. The solution obtained is then substituted into the FLS in Equation 31 that yields the required performance function.

2. Set the mean value point as an initial design point, that is, $x_{i,k} = \mu_{x_i}$ for $i = 1,2,\ldots,n$, and calculate the gradients $\nabla g(X_k)$ of the LSF at this design point. Here, $x_{i,k}$ refers to the ith element in the vector X_k of the kth iteration, and μ_{x_i} is the mean value of the ith element.

3. Calculate the initial reliability index β using the mean-value method, that is, $\beta = \frac{\mu_{\bar{g}}}{\sigma_{\bar{g}}}$ and its direction cosine α using the following equations:

$$\beta = \frac{\mu_{\bar{g}}}{\sigma_{\bar{g}}} = \frac{g(\mu_X)}{\left[\sum_{i=1}^{n}\left(\frac{\partial g(\mu_X)}{\partial x_i}\right)^2 \cdot \sigma_{xi}^2\right]^{\frac{1}{2}}} \tag{32}$$

$$\alpha_i = -\frac{\left(\frac{\partial g(X^*)}{\partial x_i}\right) \cdot \sigma_{x_i}}{\sqrt{\sum_{i=1}^{n}\left(\frac{\partial g(X^*)}{\partial x_i}\sigma_{x_i}\right)^2}}. \tag{33}$$

4. Compute a new design point X_k and U_k, function value and gradients at this new design point.

$$x_{i,k} = \mu_{x_i} + \beta\sigma_{x_i}\alpha_i \tag{34}$$

$$u_{i,k} = \frac{x_{i,k} - \mu_{x_i}}{\sigma_{x_i}} \tag{35}$$

5. Compute the reliability index β and direction cosine α_i using Equations 36 and 35, respectively.

$$\beta = \frac{g(U^*) - \sum_{i=1}^{n}\frac{\partial g(U)}{\partial x_i}\sigma_{x_i}u_i^*}{\sqrt{\sum_{i=1}^{n}\left(\frac{\partial g(U^*)}{\partial x_i}\sigma_{x_i}\right)^2}} \tag{36}$$

$$\alpha_i = -\frac{\left(\frac{\partial g(X^*)}{\partial x_i}\right) \cdot \sigma_{x_i}}{\sqrt{\sum_{i=1}^{n}\left(\frac{\partial g(X^*)}{\partial x_i}\sigma_{x_i}\right)^2}} \tag{37}$$

Repeat Steps 4 to 5 until convergence of the reliability index β is achieved.

4 | RESULTS AND DISCUSSION

4.1 | Mesh sensitivity analysis

The numerical results of fatigue analysis using finite element simulations are affected by the element size.[70] This study aims to explore the influence of various mesh sizes on fatigue life prediction. Based on the numerical results, the mesh size used is 15 μm within the pit depth vicinity (crack front) and 1000μm for the rest of the curved plate (15,1000). In this section, two more element size configurations (10, 1000) and

(20, 1000) are investigated for surface pit 223 μm at different applied loads to study the effect of the mesh size. The curves of the fatigue life predictions from the three different element sizes are plotted in Figure 5A,B for the two applied loads. Both figures reveal that the three curves obtained from different mesh sizes have a similar pattern of fatigue crack growth. Also, it can be observed that as the element size increases, the range of crack growth rate captured is wider. However, as the element size decreases a more closely spaced variation of the points is captured as against the widely dispersed captured for larger element sizes. This implies that more solution substeps are required when the element size is smaller to have the same range of crack growth rate captured by the larger element size. Also, as long as the mesh size is taken in a reasonable range, the mesh size does not affect the fatigue behaviour. Hence, fatigue behaviour can be determined solely by fatigue crack growth rate. In both figures, the curves overlap as they are in very close proximity that indicates that the element size configuration of (15, 1000) is capable of simulating the fatigue behaviours of the structure with surface corrosion pits considered in this study (in view of the element size chosen to be intermediate, trading off between capturing more points and computational cost).

4.2 | Validation of the FEA tool against experimental data

In this section, comparisons of the fatigue crack growth rate have been made between the SMART© analysis results and experimental test data found in Li and Akid[38] as the test set-up have been presented in Section 3.2.1. As depicted in Figure 6, there is a wide scatter in the fatigue crack growth rate in the threshold region for both the results predicted by the experiment and the FEA SMART© analysis tool. However, along the
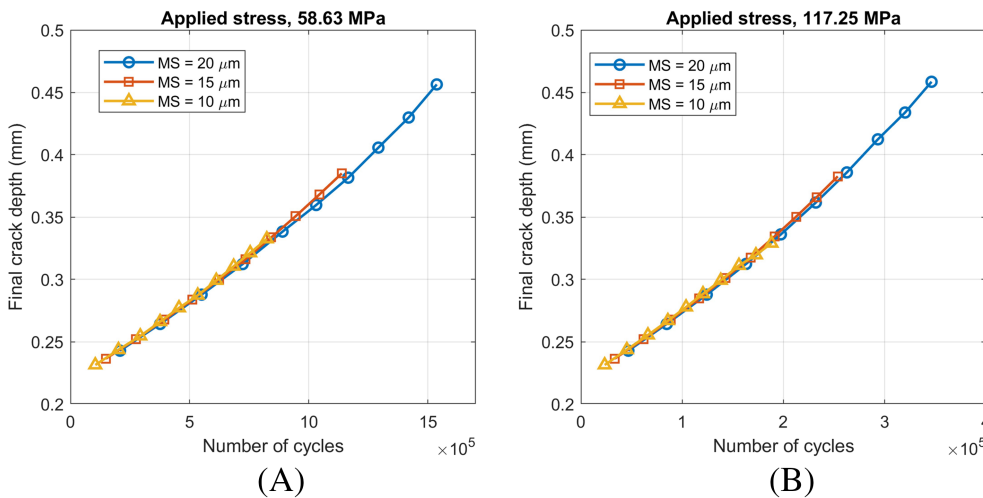

(A) (B)

FIGURE 5 Curves of fatigue life prediction obtained from different element sizes for applied stress: (A) σ = 58.63 MPa; (B) σ = 117.25 MPa [Colour figure can be viewed at wileyonlinelibrary.com]
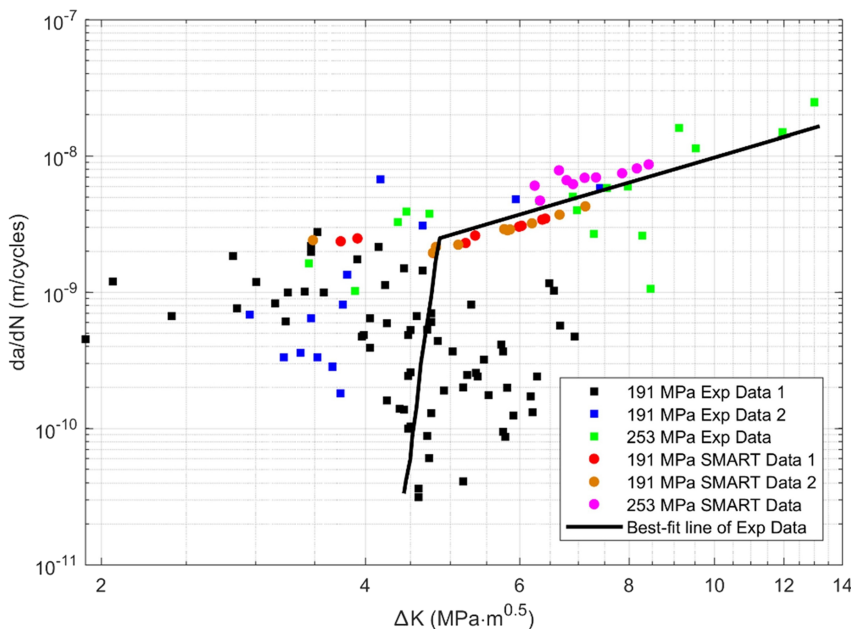

FIGURE 6 Comparison between experimental data according to Li and Akid[38] against the finite element analysis (FEA) tool adopting the same test set-up [Colour figure can be viewed at wileyonlinelibrary.com]

Paris' region, that is, after the threshold region, the test data points are seen to be dispersed around the best fit line of the experimental data such that it aligns in and can be represented by a straight line.[54,65,71–79] From the foregoing, it can be inferred that there is reasonable agreement between the test results and the FEA SMART© analysis results predicted. Hence, it can be concluded that the SMART© FEA results are acceptable due to the slight variation in results predicted by the simulation in comparison with the experimental data at the Paris' region. The transition region between the short and long crack was not predicted so well by the fatigue crack growth models. One way to address this problem is by introducing effective initial flaw size (EIFS), which is an alternative solution to the K-T diagram.[46]

4.3 | Validation of the FEA model

In this subsection, fatigue assessment is provided by a theoretical analysis, that is, according to the literature[36,37,47,64,65] and procedures given in design standard BS7910[51] for offshore structures with tubular joints, as described in Section 2.2. Based on the current SMART© analysis results, comparisons of the fatigue crack growth rate and cycle number for allowable crack growth have been made for validation.

4.3.1 | Comparison of fatigue crack growth rate

Comparisons of fatigue crack growth rate with ΔK obtained from SMART© and theoretical analysis are presented in Figure 7A,B for two surface crack geometries. For both pit sizes considered, the fatigue crack growth rate curve obtained by the SMART© analysis is close to that obtained from theoretical analysis with most of the fatigue crack growth rate of SMART© analysis points overlapping with the theoretical curve. In summary, the comparisons of fatigue crack growth rates indicate that the results obtained by SMART© are acceptable.

4.3.2 | Comparison of fatigue life

In this section, comparisons of fatigue life predictions obtained from SMART© analysis and theoretical for two different crack sizes are presented. In Figure 8A,B, it is observed that the results obtained using the two methods are very similar. From Figure 8A, it can be said that the SMART© analysis is slightly more conservative than the theoretical analysis results, whereas Figure 8B indicates otherwise. Thus, it could be explained for surface cracks, predicting the fatigue crack growth by using the theoretical method considers only the crack height's variation, whereas in the current SMART© model, the full 3-D crack is taken into account. Thus, as the crack propagates, the SMART© approach takes account of the changes in the shape factor, whereas in the theoretical analysis, this value remains constant. Hence, with SMART©, the cycle number can be reduced at a certain crack extension, in comparison with the theoretical results that show a larger value of the rate of fatigue crack growth for longer crack sizes. These results suggest that the SMART© analysis may be more reliable when compared with the theoretical analysis. It can be concluded that the fatigue crack growth behaviour of the structure with a hemispherical surface crack (corrosion pit) can be accurately predicted by the SMART© analysis tool inbuilt in ANSYS.

4.4 | Validation of the FORM

The comparison of the POF results obtained from the FORM and MCS is presented in Table 11. This was performed using a simple case assuming only the long crack growth regime life in the g-function. As can be observed, the difference in the values of POF predicted by the FORM and MCS remains consistently not more than 5%. Hence, the agreement of the two methods can be considered sufficient. Also, as can be observed, the values predicted by the FORM are more accurate for very low POF.

4.5 | Corrosion-fatigue SRA results

Time-variant corrosion-fatigue reliability assessment was carried out employing the modelling approach presented in Section 2.3. The results are presented in Figure 9. From the time-variant corrosion fatigue reliability index curve, it can be observed that the structure failed just after the 18th year as the reliability index β falls below the defined threshold of $\beta = 3.71$ as specified by DNV.[1,3,16,64] From Figure 9, it can be observed that the structural reliability prediction produced following the theoretical method gave conservative results compared with that produced using the non-intrusive formulation at the start of the through life of the structure (i.e. from Years 2 to 8) but towards the end of the design life the results may be overly optimistic. Apart from the FEA SMART model accounting for 3-D effects, this variation could be attributed to the difference in the input stochastic variables between the two methods, that is, the non-intrusive method incorporates the effects of the response of the structure to wind and hydrodynamic loads as well as soil-structure interaction. From Section 2.3 the life for the pit growth regime was calculated to be 9 years, which is almost equal to the crack propagation regimes. It can therefore be concluded that the structure's life is dominated by the pitting
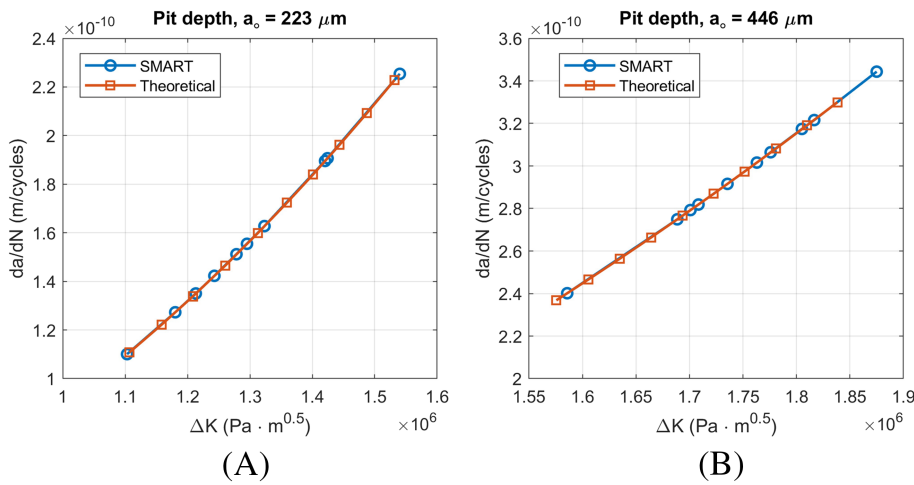
FIGURE 7 Fatigue crack growth rate with Δ obtained from SMART© and theoretical analysis respectively for (A) $a_0 = 223$ µm and (B) $a_0 = 446$ µm [Colour figure can be viewed at wileyonlinelibrary.com]

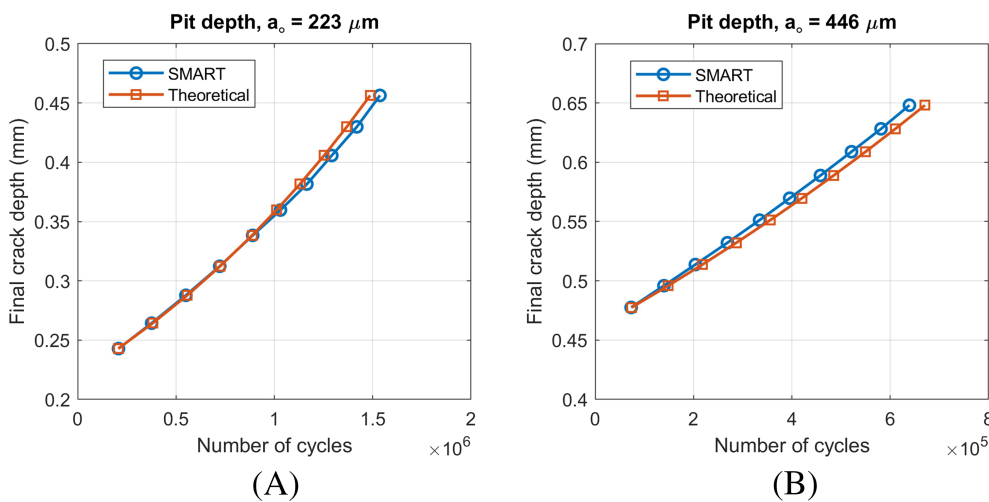**FIGURE 8** Crack heights versus the number of cycles obtained from SMART© and theoretical analysis respectively: (A) $a_0 = 223$ µm; (B) $a_0 = 446$ µm [Colour figure can be viewed at wileyonlinelibrary.com]

corrosion process. Therefore, to mitigate against the effects of corrosion fatigue, factors promoting the pitting corrosion process should be eliminated in order to increase the time to failure of the structure.

The life of the structure can be increased by extending the pit growth regime, that is, the time taken before critical pit depth is reached thus initiating the pit-to-crack transition. This can be achieved by reducing the pit current coefficient I_{po}. Practical ways of implementing this could be via the use of cathodic protection, protective coating, and/or improved scheduled inspection, maintenance and repair.

4.6 | Global sensitivity analysis

The results of a sensitivity analysis performed on the SRA using the stochastic parametric FEA are depicted in Figure 10. This depicts the most critical parameters that can radically change the response and reliability performance of the structure. It can be observed that the magnitude of

TABLE 11 Probability of failure results as predicted by the FORM and MCS

Time (years)	POF using FORM	POF using MCS	Percentage difference (%)
10	5.29E-11	0	Undefined
12	4.96E-02	0.046982	5
14	8.35E-01	0.835043	0.03
16	9.94E-01	0.996683	0.24
18	0.999917672	0.999958	4
20	0.999999999996536	1	3.46E-10

Abbreviations: FORM, first-order reliability method; MCS, Monte Carlo simulation; POF, probability of failure.

FIGURE 9 Corrosion fatigue reliability assessment [Colour figure can be viewed at wileyonlinelibrary.com]
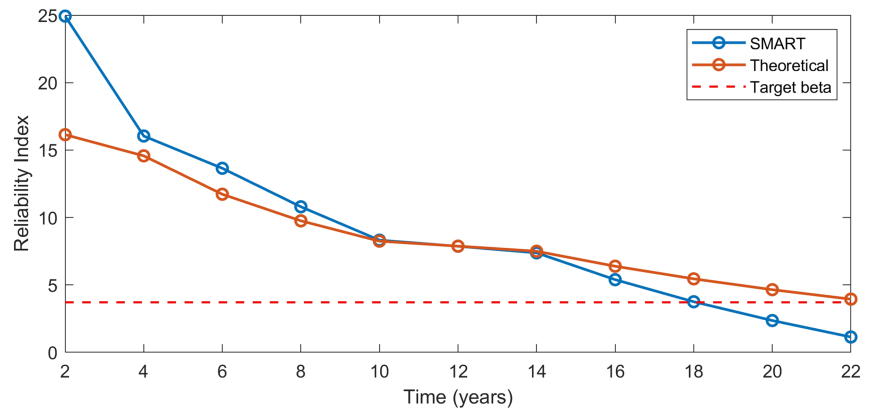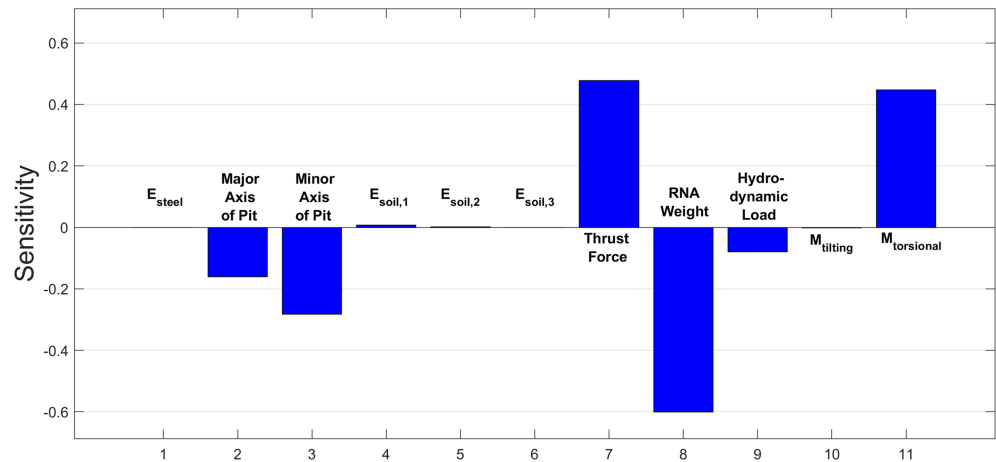

FIGURE 10 Global sensitivity analysis [Colour figure can be viewed at wileyonlinelibrary.com]

the RNA weight is the most significant and is negatively correlated. The magnitude of thrust force and the torsional moments are significant and have a positive correlation. The hydrodynamic load is negatively correlated and has little impact in comparison with the other parameters. The Young's modulus of the soil system has very little or no impact, as do the tilting moment and steel Young's modulus, whereas the other parameters major and minor radius of the pit are negatively correlated with little impact but inversely compared with the applied stress. From the analysis, it was revealed that a variation in the value of the aspect ratio of the corrosion pit at critical size (as long as size of axes are not more than the original value) leads to a corresponding variation in the reliability of the structure. Therefore, aspect ratio of pits at critical size plays a key role in the reliability of a structure.

5 | CONCLUSIONS

In this study, an SRA of an OWT support structure subjected to pitting corrosion-fatigue was performed by employing the damage tolerance model approach. The reliability assessment for the corrosion pit growth regime was performed using empirical equations from classical corrosion mechanism methodologies, whereas the SRA for crack propagation regimes, which includes the pit to small crack transition and the small crack to long crack transition regimes, was performed using a stochastic parametric FEA model. A number of structural responses corresponding to varying input stochastic parameters were predicted using high capability tools: the SMART© crack growth analysis in combination with the Design Xplorer© as packaged in ANSYS workbench. Then, these results were post-processed using an ANN surrogate modelling method to evaluate the LSF. Afterwards, the reliability index is predicted via the widely used numerical reliability techniques of FORM and MCS. The following conclusions can be drawn from the present study:

- The conducted time-variant corrosion fatigue reliability assessment method presented in this work revealed that the modelled structure is not safe after the 18th year of operation as the reliability index falls below the target reliability set at 3.71. This result is believed to be more accurate than the theoretical study, which gives 22 years.

- The structural reliability prediction produced following the theoretical method gave conservative results compared with that produced using the non-intrusive formulation during the beginning of the through life but reversed to give potentially overly optimistic results towards the end of the design life.
- The time-variant SRA carried out shows that the pitting corrosion growth regime dominates the life of the structure by 56%. The pit growth regime can be prolonged by reducing the pit current coefficient I_{po}.
- From the sensitivity analysis carried out, it was observed that a variation in the aspect ratio of the critical corrosion pit leads to a corresponding change in the structural reliability.
- The stochastic parametric FEA carried out in this study addresses the issue of randomness in the values of the shape factor, compared with the traditional methods that apply deterministic values.
- It was shown that the FEA predicts the pit accurately to small crack and small to long crack transition regimes as prescribed in classical corrosion fatigue mechanism methodology.
- The SMART© fracture FEA tool was validated against experimental data as there was agreement in the fatigue crack growth rate predicted using the same test set-up.
- Both the crack growth rate and fatigue life curves computed from the parametric FEA model show reasonable agreement with that computed using the theoretical analysis. It can be concluded that the validity of the FEA model used herein is confirmed.
- Good agreement is achieved when comparing the POF calculated for the FORM and the MCS, which implies that the numerical reliability technique employed in this study is valid.

ACKNOWLEDGEMENTS

ORCID

Abdulhakim Adeoye Shittu https://orcid.org/0000-0002-7920-6532
Ali Mehmanparast https://orcid.org/0000-0002-7099-7956
Mahmood Shafiee https://orcid.org/0000-0002-6122-5719
Athanasios Kolios https://orcid.org/0000-0001-6711-641X
Karl Pilario https://orcid.org/0000-0001-5448-0909

REFERENCES

1. Kolios A, Wang L. Advanced Reliability Assessment of Offshore Wind Turbine Monopiles by Combining Reliability Analysis Method and SHM/CM Technology. In *Proceedings of the 28th International Ocean and Polar Engineering Conference*. Japan: Sapporo; 10–15 June 2018:1412–1419.
2. IRENA. Future of wind: Deployment, investment, technology, grid integration and socio-economic aspects. In: (*A Global Energy Transformation Paper) International Renewable Energy Agency*. ; 2019.
3. Wang L, Kolios A. A generic framework for reliability assessment of offshore wind turbine monopiles considering soil-solid interaction and harsh marine environments. In: *5th International Conference on Marine Structures, MARSTRUCT*. ; 2017. https://doi.org/10.1201/9781315157368-105
4. EWEA. Offshore wind in Europe—walking the tightrope to success. *Eur Wind Energy Assoc*. Published online 2015.
5. Ioannou A, Angus A, Brennan F. A lifecycle techno-economic model of offshore wind energy for different entry and exit instances. *Appl Energy*. 2018; 221:406-424. https://doi.org/10.1016/j.apenergy.2018.03.143
6. Shittu AA, Mehmanparast A, Wang L, Salonitis K, Kolios A. Comparative study of structural reliability assessment methods for offshore wind turbine jacket support structures. *Appl Sci*. 2020;10(3):860. https://doi.org/10.3390/app10030860
7. Ziegler L, Cosack N, Kolios A, Muskulus M. Structural monitoring for lifetime extension of offshore wind monopiles: Verification of strain-based load extrapolation algorithm. *Mar Struct*. 2019;66(March):154-163. https://doi.org/10.1016/j.marstruc.2019.04.003
8. Wang X, Zeng X, Yang X, Li J. Feasibility study of offshore wind turbines with hybrid monopile foundation based on centrifuge modeling. *Appl Energy*. 2018;209:127-139. https://doi.org/10.1016/j.apenergy.2017.10.107
9. Wang X, Zeng X, Yang X, Li J. Seismic response of offshore wind turbine with hybrid monopile foundation based on centrifuge modelling. *Appl Energy*. 2019;235:1335-1350. https://doi.org/10.1016/j.apenergy.2018.11.057
10. Damiani R, Song H. A jacket sizing tool for offshore wind turbines within the systems engineering initiative. *Offshore Technol Conf*. Published Online 2013:27. https://doi.org/10.4043/24140-MS
11. Damiani RR, Song H, Robertson AN, Jonkman JM. Assessing the Importance of Nonlinearities in the Development of a Substructure Model for the Wind Turbine CAE Tool FAST. In *ASME 2013 32nd International Conference on Ocean, Offshore and Arctic Engineering*. New York, NY, USA: American Society American Society of Mechanical Engineers Digital Collection, 2013: Volume 8.
12. Dong W, Moan T, Gao Z. Fatigue reliability analysis of the jacket support structure for offshore wind turbine considering the effect of corrosion and inspection. *Reliab Eng Syst Saf*. 2012;106:11-27. https://doi.org/10.1016/j.ress.2012.06.011
13. Silva JE, Garbatov Y, Guedes SC. Reliability assessment of a steel plate subjected to distributed and localized corrosion wastage. *Eng Struct*. 2014;59: 13-20. https://doi.org/10.1016/j.engstruct.2013.10.018

14. Kim DH, Lee SG. Reliability analysis of offshore wind turbine support structures under extreme ocean environmental loads. *Renew Energy*. 2015;79(1): 161-166. https://doi.org/10.1016/j.renene.2014.11.052

15. Gholizad A, Golafshani AA, Akrami V. Structural reliability of offshore platforms considering fatigue damage and different failure scenarios. *Ocean Eng*. 2012;46:1-8. https://doi.org/10.1016/j.oceaneng.2012.01.033

16. Kolios A, Di Maio LF, Wang L, Cui L, Sheng Q. Reliability assessment of point-absorber wave energy converters. *Ocean Eng*. 2018;163 (October 2017): 40-50. https://doi.org/10.1016/j.oceaneng.2018.05.048

17. Kolios A. A Multi-Configuration Approach to Reliability Based Structural Integrity Assessment for Ultimate Strength. *Ph.D. Thesis*. Bedford, UK: Cranfield University; 2010.

18. Jiang Z, Hu W, Dong W, Gao Z, Ren Z. Structural reliability analysis of wind turbines: a review. *Energies*. 2017;10(12):1-25. https://doi.org/10.3390/en10122099

19. Wang L, Kolios A, Nishino T, Delafin PL, Bird T. Structural optimisation of vertical-axis wind turbine composite blades based on finite element analysis and genetic algorithm. *Compos Struct*. 2016;153(January 2015:123-138. https://doi.org/10.1016/j.compstruct.2016.06.003

20. Gentils T, Wang L, Kolios A. Integrated structural optimisation of offshore wind turbine support structures based on finite element analysis and genetic algorithm. *Appl Energy*. 2017;199:187-204. https://doi.org/10.1016/j.apenergy.2017.05.009

21. Wang L, Quant R, Kolios A. Fluid structure interaction modelling of horizontal-axis wind turbine blades based on CFD and FEA. *J Wind Eng Ind Aerodyn*. 2016;158:11-25. https://doi.org/10.1016/j.jweia.2016.09.006

22. Achmus M, Abdel-Rahman K. Finite element modelling of horizontally loaded monopile foundations for offshore wind energy converters in Germany. *Front Offshore Geotech*. 2005;(August 2005). doi:https://doi.org/10.1201/NOE0415390637.ch38

23. WangL, Kolios A, Delafin P-L, Nishino T, Bird T. Fluid structure interaction modelling of a novel 10MW vertical-axis wind turbine rotor based on computational fluid dynamics and finite element analysis. *Eur Wind Energy Assoc Annu Conf Exhib 2015, EWEA 2015 - Sci Proc*. 2015;44(0):

24. Yeter B, Garbatov Y, Guedes SC. Uncertainty analysis of soil-pile interactions of monopile offshore wind turbine support structures. *Appl Ocean Res*. 2019;82(November 2018):74-88. https://doi.org/10.1016/j.apor.2018.10.014

25. Jung S, Kim SR, Patil A, Hung LC. Effect of monopile foundation modeling on the structural response of a 5-MW offshore wind turbine tower. *Ocean Eng*. 2015;109:479-488. https://doi.org/10.1016/j.oceaneng.2015.09.033

26. DNV GL AS. DNVGL-ST-0126: *Support Structures for Wind Turbines*. Det Norske Veritas; 2016:182 pp. doi:https://doi.org/10.1016/j.jbiomech.2014.11.025

27. Kolios A, Srikanth S, Salonitis K. Numerical simulation of material strength deterioration due to pitting corrosion. *Procedia CIRP*. 2014;13:230-236. https://doi.org/10.1016/j.procir.2014.04.040

28. Bhandari J, Khan F, Abbassi R, Garaniya V, Ojeda R. Modelling of pitting corrosion in marine and offshore steel structures—a technical review. *J Loss Prev Process Ind*. 2015;37:39-62. https://doi.org/10.1016/j.jlp.2015.06.008

29. Larrosa NO, Akid R, Ainsworth RA. Corrosion-fatigue: a review of damage tolerance models. *Int Mater Rev*. 2018;63(5):283-308. https://doi.org/10.1080/09506608.2017.1375644

30. McCulloch WS, Pitts W. A logical calculus of the ideas immanent in nervous activity. *Bull Math Biophys*. 1943;5(4):115-133. https://doi.org/10.1007/BF02478259

31. Hornik K, Stinchcombe M, White H. Multilayer feedforward networks are universal approximators. *Neural Netw*. 1989;2(5):359-366. https://doi.org/10.1016/0893-6080(89)90020-8

32. Bucher C, Most T. A comparison of approximate response functions in structural reliability analysis. *Probabilistic Eng Mech*. 2008;23(2–3):154-163. https://doi.org/10.1016/j.probengmech.2007.12.022

33. Hosni Elhewy A, Mesbahi E, Pu Y. Reliability analysis of structures using neural network method. *Probabilistic Eng Mech*. 2006;21(1):44-53. https://doi.org/10.1016/J.PROBENGMECH.2005.07.002

34. Gomes HM, Awruch AM. Comparison of response surface and neural network with other methods for structural reliability analysis. *Struct Saf*. 2004; 26(1):49-67. https://doi.org/10.1016/S0167-4730(03)00022-5

35. Chojaczyk AA, Teixeira AP, Neves LC, Cardoso JB, Guedes SC. Review and application of artificial neural networks models in reliability analysis of steel structures. *Struct Saf*. 2015;52(PA:78-89. https://doi.org/10.1016/j.strusafe.2014.09.002

36. Cardoso JB, de Almeida JR, Dias JM, Coelho PG. Structural reliability analysis using Monte Carlo simulation and neural networks. *Adv Eng Softw*. 2008; 39(6):505-513. https://doi.org/10.1016/J.ADVENGSOFT.2007.03.015

37. Shi P, Mahadevan S. Damage tolerance approach for probabilistic pitting corrosion fatigue life prediction. *Eng Fract Mech*. 2001;68(13):1493-1507. https://doi.org/10.1016/S0013-7944(01)00041-8

38. Li SX, Akid R. Corrosion fatigue life prediction of a steel shaft material in seawater. *Eng Fail Anal*. 2013;34:324-334. https://doi.org/10.1016/j.engfailanal.2013.08.004

39. Kondo Y. Prediction of fatigue crack initiation life based on pit growth. *Corrosion*. 1989;45(1):7-11. https://doi.org/10.5006/1.3577891

40. Wang QY, Pidaparti RM, Palakal MJ. Comparative study of corrosion-fatigue in aircraft materials. *AIAA j*. 2012;39(2):325-330. https://doi.org/10.2514/3.14734

41. Rokhlin SI, Kim JY, Nagy H, Zoofan B. Effect of pitting corrosion on fatigue crack initiation and fatigue life. *Eng Fract Mech*. 1999;62(4–5):425-444. https://doi.org/10.1016/S0013-7944(98)00101-5

42. Sriraman MR, Pidaparti RM. Crack initiation life of materials under combined pitting corrosion and cyclic loading. *J Mater Eng Perform*. 2010;19(1): 7-12. https://doi.org/10.1007/s11665-009-9379-9

43. Sriraman MR, Pidaparti RM. Life prediction of aircraft aluminum subjected to pitting corrosion under fatigue conditions. *J Aircr*. 2009;46(4): 1253-1259. https://doi.org/10.2514/1.40481

44. Wu X. Short fatigue crack behaviour of a submarine hull steel in inert and aggressive environments. University of Sheffield, PhD Dissertation; 1995.

45. Xue Y. Modeling fatigue small-crack growth with confidence—a multistage approach. *Int J Fatigue*. 2010;32(7):1210-1219. https://doi.org/10.1016/J.IJFATIGUE.2009.12.016

46. Morse L, Khodaei ZS, Aliabadi MH. A multi-fidelity modelling approach to the statistical inference of the equivalent initial flaw size distribution for multiple-site damage. *Int J Fatigue*. 2019;120(November 2018:329-341. https://doi.org/10.1016/j.ijfatigue.2018.11.010

47. Morse L, Sharif Khodaei Z, Aliabadi MH. A multi-fidelity boundary element method for structural reliability analysis with higher-order sensitivities. *Eng Anal Bound Elem*. 2019;104 (April):183-196. https://doi.org/10.1016/j.enganabound.2019.03.036

48. Choi S-K, Grandhi R, Canfield R. *Reliability-Based Structural Design*. London: Springer-Verlag; 2007.

49. ANSYS. White Paper: SMART Fracture.; 2018.

50. Anderson TL. *Fracture Mechanics Fundamentals and Applications*. Third Boca Raton, FL: Taylor and Francis; 2005.

51. BS 7910. *BSI Standards Publication Guide to Methods for Assessing the Acceptability of Flaws in Metallic Structures*. UK: BSI Stand Publ; 2015:490.

52. Saha JK. *Corrosion of constructional steels in marine and industrial environment: frontier work in atmospheric corrosion*. Springer; 2013. https://doi.org/10.1007/978-81-322-0720-7

53. Cerit M, Genel K, Eksi S. Numerical investigation on stress concentration of corrosion pit. *Eng Fail Anal*. 2009;16(7):2467-2472. https://doi.org/10.1016/j.engfailanal.2009.04.004

54. Igwemezie V, Mehmanparast A, Kolios A. Materials selection for XL wind turbine support structures: A corrosion-fatigue perspective. *Mar Struct*. 2018;61(December 2017:381-397. https://doi.org/10.1016/j.marstruc.2018.06.008

55. Martinez-Luengo M, Kolios A, Wang L. Parametric FEA modelling of offshore wind turbine support structures: Towards scaling-up and CAPEX reduction. *Int J Mar Energy*. 2017;19(2017):16-31. https://doi.org/10.1016/j.ijome.2017.05.005

56. Drucker D, Prager W. Soil mechanics and plastic analysis or limit design. *Q Appl Math*. 1952;10(2):157-165.

57. Damiani R. JacketSE. : An offshore wind turbine jacket sizing tool theory manual and sample usage with preliminary validation. Report: NREL/TP-5000-65417, National renewable energy laboratory (NREL), Denver West Parkway Golden, CO, USA; 2016.

58. IEC. IEC 61400–1: Wind turbines part 1: design requirements. Published online 2005.

59. Det Norske Veritas (DNV). DNV-OS-J101 design of offshore wind turbine structures. *May*. 2014;(May):212–214.

60. Sarpkaya TS. *Wave Forces on Offshore Structures*. Cambridge University Press; 2010. https://doi.org/10.1017/CBO9781139195898

61. Hassan T, Liu Z. On the difference of fatigue strengths from rotating bending, four-point bending, and cantilever bending tests. *Int J Press Vessel pip*. 2001;78(1):19-30. https://doi.org/10.1016/S0308-0161(00)00080-6

62. Pook LP. *Linear Elastic Fracture Mechanics for Engineers: Theory and Applications*. WIT Press; 2000.

63. Kühn M. Dynamics and Design Optimization of Offshore Wind Energy Conversion Systems; DUWIND, Delft University Wind Energy Research Institute; 1999.

64. (DNV) Det Norske Veritas. Structural reliability analysis of marine structures. *DNV CN 30–6*. Published online 1992.

65. Yeter B, Garbatov Y, Soares CG. Reliability of Offshore Wind Turbine Support Structures Subjected to Extreme Wave-Induced Loads and Defects. In: *Proceedings of the ASME 2016 35th International Conference on Ocean*. Busan, Korea: Offshore and Arctic Engineering OMAE2016-54240; 2016:1-8.

66. BSI. BS EN 1990 Eurocode. : Basis of structural design *Br Stand Inst* Published Online 2002.

67. Reh S, Beley JD, Mukherjee S, Khor EH. Probabilistic finite element analysis using ANSYS. *Struct Saf*. 2006;28(1–2):17-43. https://doi.org/10.1016/j.strusafe.2005.03.010

68. ANSYS. DesignXplorer user's guide. Published online 2018.

69. Hasofer A, Lind N. An exact and invariant second moment code format. *J Engrg Mech Div ASCE*. 1974;100(1):111-121.

70. Zhang YM, Fan M, Xiao ZM, Zhang WG. Fatigue analysis on offshore pipelines with embedded cracks. *Ocean Eng*. 2016;117 (May):45-56. https://doi.org/10.1016/j.oceaneng.2016.03.038

71. Adedipe O, Brennan F, Mehmanparast A, Kolios A, Tavares I. Corrosion fatigue crack growth mechanisms in offshore monopile steel weldments. *Fatigue Fract Eng Mater Struct*. 2017;40(11):1868-1881. https://doi.org/10.1111/ffe.12606

72. Mehmanparast A, Brennan F, Tavares I. Fatigue crack growth rates for offshore wind monopile weldments in air and seawater: SLIC inter-laboratory test results. *Mater des*. 2017;114:494-504. https://doi.org/10.1016/j.matdes.2016.10.070

73. IgwemezieV, Mehmanparast A. Waveform and frequency effects on corrosion-fatigue crack growth behaviour in modern marine steels. *Int J Fatigue*. 2020;134:105484. https://doi.org/10.1016/j.ijfatigue.2020.105484

74. Igwemezie V, Dirisu P, Mehmanparast A. Critical assessment of the fatigue crack growth rate sensitivity to material microstructure in ferrite-pearlite steels in air and marine environment. *Mater Sci Eng a*. 2019;754:750-765. https://doi.org/10.1016/j.msea.2019.03.093

75. Jacob A, Oliveira J, Mehmanparast A, Hosseinzadeh F, Kelleher J, Berto F. Residual stress measurements in offshore wind monopile weldments using neutron diffraction technique and contour method. *Theor Appl Fract Mech*. 2018;96:418-427. https://doi.org/10.1016/j.tafmec.2018.06.001

76. JacobA, Mehmanparast A, D'Urzo R, Kelleher J. Experimental and numerical investigation of residual stress effects on fatigue crack growth behaviour of S355 steel weldments. *Int J Fatigue*. 2019;128:105196. https://doi.org/10.1016/j.ijfatigue.2019.105196

77. ASTM. ASTM E647: Standard test method for measurement of fatigue crack growth rates. Published online 2016. https://doi.org/10.1520/E0647-15E01.2

78. Mehmanparast A, Taylor J, Brennan F, Tavares I. Experimental investigation of mechanical and fracture properties of offshore wind monopile weldments: SLIC interlaboratory test results. *Fatigue & Fracture of Engineering Materials & Structures*. 2018;41(12):2485-2501. https://doi.org/10.1111/ffe.12850

79. Fisher T, De Vries W, Schmidt B. Upwind design basis (WP4 offshore foundations and support structures). Published Online 2010. https://repository.tudelft.nl/islandora/object/uuid%3Aa176334d-6391-4821-8c5f-9c91b6b32a27 (accessed on 4 June 2019).